Structural Engineering and Mechanics, *Vol. 74, No. 2 (2020) 283-296*
DOI: https://doi.org/10.12989/sem.2020.74.2.283

Study on rock fracture behavior under hydromechanical loading by 3-D digital reconstruction

Miaomiao Kou[1,2,3a], Xinrong Liu*[1] and Yunteng Wang[1b]

[1]*School of Civil Engineering, Chongqing University, Chongqing, 400045, China;*
[2]*School of Civil Engineering, Qingdao University of Technology, Qingdao, 266033, China;*
[3]*Cooperative Innovation Center of Engineering Construction and Safety in Shandong Blue Economic Zone, Qingdao, 266033, China*

(Received October 26, 2019, Revised November 30, 2019, Accepted December 12, 2019)

Abstract. The coupled hydro-mechanical loading conditions commonly occur in the geothermal and petroleum engineering projects, which is significantly important influence on the stability of rock masses. In this article, the influence of flaw inclination angle of fracture behaviors in rock-like materials subjected to both mechanical loads and internal hydraulic pressures is experimentally studied using the 3-D X-ray computed tomography combined with 3-D reconstruction techniques. Triaxial compression experiments under confining pressure of 8.0 MPa are first conducted for intact rock-like specimens using a rock mechanics testing system. Four pre-flawed rock-like specimens containing a single open flaw with different inclination angle under the coupled hydro-mechanical loading conditions are carried out. Then, the broken pre-flawed rock-like specimens are analyzed using a 3-D X-ray computed tomography (CT) scanning system. Subsequently, the internal damage behaviors of failed pre-flawed rock-like specimens are evaluated by the 3-D reconstruction techniques, according to the horizontal and vertical cross-sectional CT images. The present experimental does not only focus on the mechanical responses, but also pays attentions to the internal fracture characteristics of rock-like materials under the coupled hydro-mechanical loading conditions. The conclusion remarks are significant for predicting the rock instability in geothermal and unconventional petroleum engineering.

Keywords: hydro-mechanical loading; flaw inclination angle; internal fracture behaviors; rock-like materials; 3-D reconstruction

1. Introduction

In rock masses, there exist large numbers of discontinuous structures, such as joints, flaws, faults, etc. (Wong *et al*. 1998; Bobet and Einstein 1998; Christe *et al*. 2011; Cao *et al*. 2018), which are the weak parts of surrounding rocks in different rock engineering projects, such as geothermal extraction, unconventional petroleum exploitation, tunneling excavation, etc (Bobet and Einstein 1998; Cao *et al*. 2018; Cheng *et al*. 2016; Cała *et al*. 2016; Haeri *et al*. 2018, 2019a, b; Wang *et al*. 2020). In some rock engineering projects, rock masses usually exist in the environments under the coupled hydro-mechanical loading conditions (Cała *et al*. 2016; Diaz *et al*. 2017; Einstein and Hirschfeld 1973; Kou *et al*. 2019a, b). On one hand, the fracture characteristics of rock materials containing flaws could result in the rock failure and engineering instability in mining and tunneling excavations under the coupled hydro-mechanical loading conditions. For example, the influence of hydro-mechanical loads on the strength and stability of rock masses in the submarine tunnel excavations and mining excavations in Karst cave area (Ge *et al*. 2001). On the other hand, the reasonable utilization of rock hydro-mechanical fracture process could help to improve the energy exploitations in geothermal and petroleum engineering projects. For instance, internal hydraulic pressures in naturally open flaws significantly affect the hydraulic fracture techniques in the unconventional petroleum exploitation (Hirono *et al*. 2003; Huang *et al*. 2017a, b, 2018a, b; Haeri *et al*. 2019b). Compared with numerical simulations and theory analysis (Wang *et al*. 2016, 2017, 2018a, b, c, d, 2019a, b, c, d, e, f; Song *et al*. 2019a; Kou *et al*. 2019b, c), laboratory experiments directly provide physical mechanism of phenomena. Therefore, it is an important issue to investigate the fracture process and failure mechanism of rocks subjected to both mechanical loads and internal hydraulic pressures (Huang *et al*. 2017b, 2018a, b).

As a non-destructive technique, such as digital image correlation (Yu and Pan 2017; Yu *et al*. 2019; Zhou *et al*. 2019) the ability of imaging detailed material information, X-ray CT scanning technique has the ability of gaining observations of the evolution and propagation of defects in the internal materials, which has been widely applied in rock and rock-like materials (Cała *et al*. 2016; Sufian and Russell 2013; Silva *et al*. 2014; Kawakata *et al*. 1999; Meier *et al*. 2015; Liu *et al*. 2018; Wang *et al*. 2016, 2017, 2018a, 2019a; Li and Chen 2016, 2017a, b). The internal geometrical and internal fracture patterns of geomaterials,

*Corresponding author, Ph.D.
E-mail: liuxrong@126.com
[a] Ph.D., Associate Professor
E-mail: koumiaomiao@qut.edu.cn
[b] Ph.D., Post-Doctoral Fellow
E-mail: yunteng.wang@kaust.edu.sa

ISSN: 1225-4568 (Print), 1598-6217 (Online)

such as pores, non-uniform distribution of natural fractures, bedding plane, grain boundaries, fossils, inclusions, mineral cleavage planes and micro-cracks, can be investigated using the X-ray CT scanning system. Christe *et al*. (2011) applied the X-ray CT-based index to characterize the quality of cataclastic carbonate rock samples. Zhang *et al*. (2019) investigated the ultimate failure modes in three different rock materials using X-ray CT scanning system combined with reconstructions. The assessment of anisotropy in rocks by systematic and planar clustering of 3-D X-ray attenuation values and associated statistical analysis on the basis that X-ray CT images directly represent the internal density of the mineral fabric in the rock mass by Yun *et al* .(2013). Furthermore, some scholars also successfully applied the X-ray CT scanning technique to investigate the internal crack initiation, propagation and coalescence characteristics of geomaterials specimens under the various uniaxial compressive tests (Yang *et al*. 2016, 2018; Wang *et al*. 2018a, 2019a, b, c, e, 2020). To explore the evolution characteristics of internal damage and fracture patterns of rocks under different loading conditions, the loading and unloading fracture mechanical tests of rocks were conducted using X-ray CT scanning images by Zhou *et al*. (2008) The fracture behaviors of Westerly granite under uniaxial and triaxial compressive conditions were analyzed using the X-ray CT scanning system by Kawakata *et al*. (1999). Based on the X-ray CT scanning system, Sufian and Russell (2013) investigated the micro-structural pore changes and energy dissipation in Gosford sandstone during pre-failure loading, but the stress condition was restricted to uniaxial compression. Zhao *et al*. (2014) employed the X-ray CT observation to analyze the mechanism of Gosford sandstone under uniaxial compression with different strain rates. The real-time high-resolution X-ray CT was applied to study deformation and failure characteristics of shale samples and bimsoil specimens under unconfined axial compressions by Wang *et al*. (2018a, 2019a, c). Since the X-ray CT scanning system is difficult to be applied in the triaxial compressive processes, the aforementioned previous studies of investigating the real-time fracturing process of geomaterials, such as soils, rock materials and rock-like materials, are mainly focused on the uniaxial compressive conditions (Wang *et al*. 2017, 2019b; Yang *et al*. 2016; Yang 2018; Song *et al*. 2018, 2019b).

To study the internal fracture behaviors of rock and rock-like materials in the triaxial compression, some scholars applied the X-ray CT system to investigate fracture behaviors of rock and rock-like materials at the different loading stages. Cała *et al*. (2016) used the X-ray CT scanning system to study fracture characteristics of gas shale at the end of three different loading stages. They determined the mechanism of shale failure, shale failure geometry and shale mechanical properties in experiments. The strength, deformability and X-ray CT observations of deeply buried marble under different confining pressures are experimentally researched by X-ray CT scanning technique with 3-D reconstruction by Yang *et al*. (2016) to investigate the 3-D ultimate failure patterns (Yang 2018). Soon afterwards, Yang and Huang (2017) investigated the effects of confining pressures and fissure angle on the internal crack evolution behaviors of sandstones using X-ray CT technique in the laboratory. Yang (2018) analyzed the compressed hollow-cylinder sandstone specimens using the three-dimensional (3-D) X-ray CT scanning system, which provides the internal crack evolution mechanism of hollow-cylinder sandstone specimens in the conventional triaxial compression experiments. However, to the best knowledge of authors, few studies of the hydro-mechanical fracture characteristics in rock-like materials were conducted using the X-ray CT scanning system combined with the 3-D reconstruction technique, which can provide the visible 3-D fracture surfaces in the rock-like specimens.

In the present research, a new steel mold is designed to fabricate the ISRM standard rock-like cylinder specimens containing the single pre-existing flaw and the water guiding hole. The influence of flaw inclination angle on the fracture and permeability evolutions in the pre-flawed rock-like cylindrical specimens subjected to both mechanical loads and internal hydraulic pressures is investigated. The pre-flawed rock-like specimen with inclination angle of 45^{o} under the conventional triaxial compression is conducted to be as a reference example. In the present experiments, the axial stress and confining pressures are first simultaneously applied to the pre-flawed rock-like specimens until the confining pressures reach 8.0 MPa. Then, the confining pressures are kept as constants, while, the axial stresses continue to apply on the pre-flawed rock-like specimens until the failure occurs. Meanwhile, the internal hydraulic pressure of 2.0 MPa is applied to surfaces of the pre-existing flaw through the water guiding hole in the pre-flawed rock-like specimens. The confining pressure of 8.0 MPa and internal hydraulic pressure of 2.0 MPa are selected based on the actual monitoring data in the rock engineering project in Three Gorges Reservoir Region, Chongqing City, China. The X-ray CT scanning system is subsequently employed to analyze internal fracture characteristics of failed rock-like specimens. Based on the X-ray CT scanning images, 3-D fracture surfaces in the spatial distributions and the associated fracture mechanism in different broken rock-like specimens are revealed through 3-D reconstruction technique. The X-ray CT scanning system combined with 3-D reconstruction provide some new internal insights of fracture mechanism of rock-like materials subjected to both the mechanical loads and internal hydraulic pressures. The present experimental results may be helpful in designing different rock engineering projects, as well as in fracturing processes.

The following structure of this paper is outlined as follows. In Section 2, the experimental methodologies, including rock-like specimen preparations, testing procedures and experimental devices, are presented. Experimental results, such as strength, deformability, surface failure patterns, and internal fracture modes, in the pre-flawed rock-like specimens under the coupled hydro-mechanical loading conditions are shown in Section 3. Finally, conclusion remarks of flaw inclination angle on fracture behaviors in pre-flawed rock-like specimens subjected to both mechanical loads and internal hydraulic pressures are drawn in Section 4.

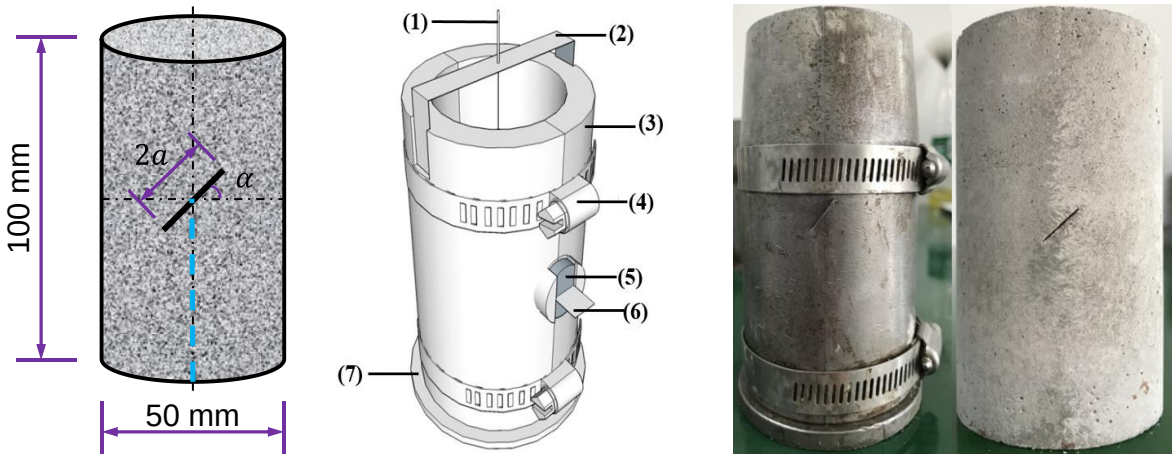

(a) (b) (c)

Fig. 1 (a) The pre-flawed rock-like specimen geometries, (b) new designing steel mold and (c) actual images

2. Experimental methodology

2.1 Specimen preparations

It is difficult, tedious and time-consuming to fabricate pre-existing flaws in natural rock materials (Cao *et al*. 2018; Liu *et al*. 2018; Zhou *et al*. 2019). The preflawed rock specimens in laboratory experiments are often replaced by the synthetic rock-like materials (Einstein and Hirschfeld 1973; Wong and Chau 1998; Bobet and Einstein 1998; Cao *et al*. 2018a, b; Liu *et al*. 2018; Wong and Einstein 2009; Zhou *et al*. 2014, 2019; Wang *et al*. 2019a; Zhuang *et al*. 2014). In this study, rock-like materials are made of cement, fine sand, rubber powder, water and some additives. On the basis of a great amount of trial and error calibration tests, the final proportion of ingredients are determined, and the mechanical parameters of such proportions produces rock-like materials similar to sandstone as listed in Table 1 through the basic rock experiments. The synthetic rock-like materials are prepared with silica sand, No. 42.5 Poland cement, water and rubber powder at mass ratio of 1.0: 0.8: 0.35: 0.12.

All the triaxial experiments are conducted on the pre-fissured cylindrical rock-like specimens 50 mm in diameter and 100 mm in length, as shown in Fig. 1(a). The new steel mold is designed to directly fabricate the rock-like specimens containing a single flaw and a guiding water hole, as shown in Fig. 1(b). It can be observed from Fig. 1(b) that the new designed steel mold consists of seven different parts, including (1) steel column, (2) curved thin steel plate, (3) steel hollow cylinder, (4) hose clamps, (5) swivel plate, (6) straight thin steel plate and (7) pedestal. The length and width of the straight thin steel plate are equal to 10 mm and 0.8 mm, which are used to determine the length and width of the single pre-existing flaw in rock-like cylinder specimens, as shown in Fig. 1(c). The swivel plate in the new designed mold make it be possible to fabricate pre-flawed rock-like specimens with different flaw inclination angle. The diameter of steel column is 0.3 mm, which is used to determine geometry of guiding water hole in the pre-flawed rock-like specimens, as shown in Fig. 1.

Table 1 The average physical parameters of rock-like materials obtained from experiments

Parameters	Rock-like material	Sandstone (Zhuang *et al*. 2014)
Density, ρ (g/cm^3)	2.15	2.20-2.71
Young's modulus, E (GPa)	15.43	3-35
Poisson ratio, υ	0.183	0.02-0.2
Cohesion strength, c (MPa)	17.96	4-40
Friction angle, ϕ (°)	25.11	25-60
Uniaxial compressive strength, σ_c (MPa)	55.28	20-170
Tensile strength, σ_t (MPa)	5.88	4-25

In the present study, to investigate the effect of flaw inclination angle on the hydro-mechanical fracture behaviors in rock-like cylinder specimens. The flaw inclination angles in four different types of pre-flawed rock-like specimen are 0°, 30°, 45° to 60°. The length and width of the single pre-existing flaw are equal to 2a=10 mm and 0.8 mm, respectively. The length of guiding water hole is 50 mm, and the diameter of guiding water hole equates to 0.3 mm. In the process of fabricating pre-flawed rock-like cylinder specimens, the mold with the fresh rock-like materials is vibrated to minimize the air bubbles for 10 min on a shaking table. The straight thin steel plates and the steel columns are disassembled after 12 h of curing, and the steel hollow cylinders are removed after 24 h of curing. All the specimens taken out from the steel mold are stored in a special curing room with temperature of 20 °C, the relative humidity of 95% and an atmospheric pressure for 28 days. For the sake of keeping mechanical properties of pre-flawed rock-like specimens as consistent as possible, the mix proportion of synthetic rock-like materials remains the same and the preparation processes are carefully controlled. Before the hydro-mechanical fracture tests, all pre-flawed rock-like specimens are stored in SRH Intelligent Vacuum Saturator to ensure the pre-flawed rock-like specimens to be vacuum and saturated states, which is used to prevent the occurrence of fluid flow in the rock-like matrixes.

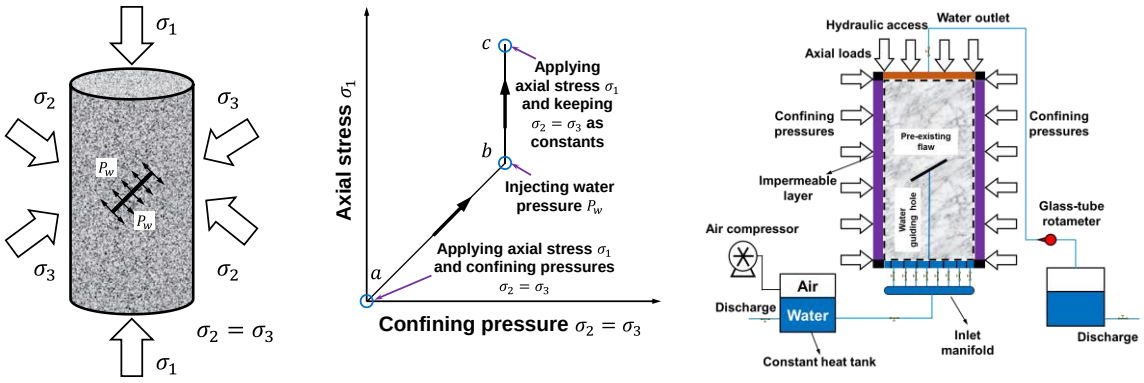

(a) (b) (c)

Fig. 2 The coupled hydro-mechanical loading conditions including (a) the loading schematic of a pre-flawed rock-like specimen, (b) loading paths and (c) testing equipment

2.2 Testing procedure

In the present study, the pre-flawed rock-like specimens with different inclination angles are subjected to not only the mechanical loads, including axial stress and confining pressures, but also the internal hydraulic pressures on the surfaces of pre-existing flaw. The schematic diagram of the pre-flawed rock-like specimens under the coupled hydro-mechanical loading conditions is performed in Fig. 2(a). Furthermore, the confining pressure and the internal hydraulic pressure are fixed as 8.0 MPa and 2.0 MPa, respectively, in the present research. To realize the coupled hydro-mechanical loading conditions of pre-flawed rock-like specimens, it can be found from Fig. 2(b) that the loading paths in this study can be divided into two loading stages as follows:

(1) The axial stresses and confining pressures are simultaneously applied on the pre-flawed specimens using the load-controlled loading type at the same rate, as shown in Fig. 2(b).

(2) When the confining pressures and axial stresses reach the preset value, i.e., 8.0 MPa, the confining pressures on the pre-flawed rock-like specimens are kept as constants. While, the axial stresses continue to be applied on the pre-flawed rock-like specimens, as shown in Fig. 2(b). At the same time, it can also be found from Fig. 2(b) that the internal hydraulic pressures on the surfaces of pre-existing flaws are applied through the guiding water holes in the pre-flawed rock-like specimens.

To investigate the fracture mechanism of pre-flawed rock-like specimens under the hydro-mechanical loading conditions, the tested pre-flawed rock-like specimens are categorized into two groups. In the first group, the pre-flawed rock-like specimen with $\alpha = 45°$ is only subjected to the mechanical loads, which is used as a reference example to illustrate the internal hydraulic effects. In the second group, the pre-flawed rock-like specimen with different flaw inclination angles are subjected to both the mechanical loads and internal hydraulic pressures. In addition, the hydro-mechanical loading conditions in the second group of pre-flawed rock-like specimens are same. The geometrical and loading conditions are summarized in Table 2.

Table 2 Geometrical and loading parameters of pre-flawed rock-like cylindrical specimens

Group	Type	Flaw length	Flaw inclination angle	Confining pressures	Internal hydraulic pressure
Group 1	Type-I	10 mm	45°	8.0 MPa	0.0 MPa
Group 2	Type-II	10 mm	45°		2.0 MPa
	Type-III	10 mm	0°		
	Type-IV	10 mm	30°		
	Type-V	10 mm	60°		

2.3 Laboratory testing devices

The conventional triaxial compression experiments on the preflawed rock-like specimens under the coupled hydro-mechanical loading conditions are carried out with rock multi-field coupling triaxial apparatus, i.e., TRIAXIAL CELL V4.0, produced by Top Industries, as shown in Fig. 2(c). The present exquipment consists of a loading system, the confining oil pressure system, the water flow pressure system and an automatic data collection system. To maintain constant water feed pressure, water in the large tank was pressurised by compressed air. A high-strength rubber bladder was used inside the tank to separate air from pressurised water and hence prevent air dissolving into water under high pressure, as shown in Fig. 2(c). This expeirmental apparatus is suitable to test mechanical responses of rock-like materials under the coupled thermo-hydro-chemo-mechanical loading conditions. The maximum loading capacity of the servo-controlled system is 1000 kN, the maximum confining pressure is 60 MPa, and the maximum pore fluid pressure is equal to 60MPa. During the experimental process, the axial force, axial deformation and radial deformation can also be measured using the present experimental apparatus. Furthermore, the confining pressures $\sigma_2 = \sigma_3$ and axial stresses σ_1 are first applied at the rate of 1.0 MPa/min at the first loading stage during experiments. Subsequently, the confining pressures $\sigma_2 = \sigma_3$ are kept as 8.0 MPa, and the axial stresses σ_1

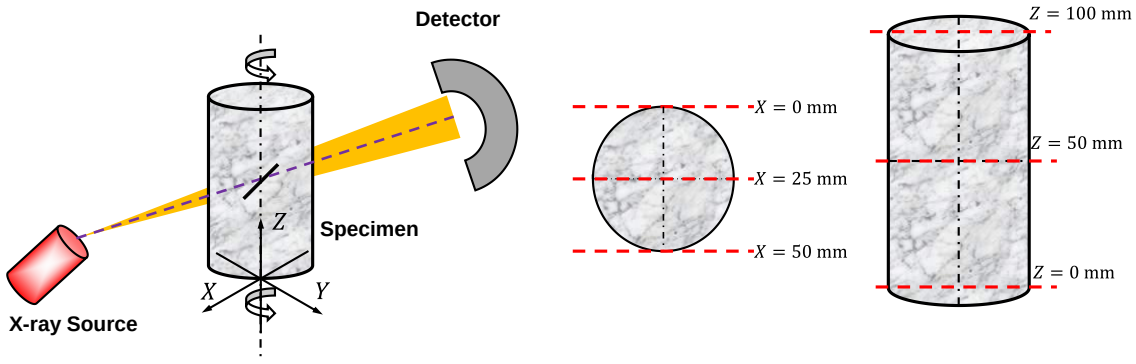

(a) (b) (c)

Fig. 3 The schematic of X-ray CT scanning system, including (a) test illustration, (b) vertical slices of cross sections and (c) horizontal slices of crack sections.

continue to be applied on the pre-flawed rock-like specimen at the rate of 0.01 mm/min until the occurrence of failure at the second loading stage. Meanwhile, the internal hydraulic pressure $P_w = 2.0$ MPa is applied on the surfaces of pre-existing flaws through the guiding water hole at the second loading stage. It should be noted that the internal hydraulic pressure is lower than the confining oil pressure in all tests, which is used to prevent the fluid flow along the surface of pre-existing flaw.

The X-ray CT scanning system is carried out on the broken rock-like specimens using a SIEMENS-SOMATOM scope X-ray CT scanner, as shown in Fig. 3(a). The X-rays are produced by electrons striking a Mo-W alloy target in an X-ray tube. The electron current is set as 81 μA and the accelerating voltage is employed as 130 kV. The present X-ray CT scanner has the spatial resolution of $0.35\ \text{mm} \times 0.35\ \text{mm}$, and scanning time of X-ray CT scanner is 1500 ms for a single slice. For the vertical cross section in Fig. 3(b), the slice images are captured at 0.8 mm, as shown in Fig. 3(b). Similarly, for the horizontal cross section in Fig. 3(c), slice interval thickness is equal to 0.64 mm. The working principles of X-ray CT scanning procedure are also summarized in Fig. 3(c). In the X-ray CT-scanning tests, failed specimens under different hydro-mechanical loading conditions are scanned. 158 slices can be obtained for every failed specimen. Moreover, the size of each X-ray CT image is 512×512 pixels, and the region of interest with a size of 141×141 pixels can be cropped from the original image to process the 3-D reconstruction using the commercial software Avizo.

3. Results and discussions

In this section, the experimental results are analyzed from two different fields, including mechanical and deformation behaviors and macroscopic fracture characteristics, in the pre-flawed rock-like specimens subjected to both mechanical loads and internal hydraulic pressures.

3.1 Mechanical and deformation behaviors

To first illustrate the effect of internal hydraulic pressure on the mechanical and deformation of pre-flawed rock-like specimens, two types of pre-flawed rock-like specimens containing a single pre-existing flaw with $\alpha = 45°$ under the fixed confining pressure of 8.0 MPa are conducted. The first type of pre-flawed rock-like specimen is only subjected to the mechanical loads. While, the second type of pre-flawed rock-like specimen is subjected to both mechanical loads and the internal hydraulic pressure of 2.0 MPa. In this study, σ_1 and σ_3 represent the axial stress (i.e., major principal stress) and the confining pressure, respectively. ε_1 and ε_3 are denoted as the axial strain and the lateral strain, respectively.

The deviatoric stress–axial strain curves of the above two types of pre-flawed rock-like specimens are plotted in Fig. 4. Compared with the uniaxial compressive strength (UCS) of intact rock-like cylinder specimen (average value), which is equal to 55.28 MPa in Table 1, it can be found that from Fig. 4 that the traixial compressive strengths of pre-flawed rock-like specimens are significantly affected by the internal hydraulic pressures. As shown in Fig. 4, the triaxial compressive strengths pre-flawed rock-like specimens decreases with increasing the internal hydraulic pressures under the fixed confining pressure of 8.0 MPa. The peak axial strain of pre-flawed rock-like specimen subjected to internal hydraulic pressure of 2.0 MPa is smaller than that under the condition of no internal hydraulic pressure. While, it can be found from Fig. 4 that the peak lateral strain of pre-flawed rock-like specimen subjected to internal hydraulic pressure of 2.0 MPa is larger than that subjected to internal hydraulic pressure of 0.0 MPa. This phenomena indicates that the internal hydraulic pressure contributes to the lateral deformation and prevent the axial deformation under the fixed confining pressure. Furthermore, it can be also found from Fig. 4 that the degree of strain softening in the post-peak deformation region decreases as the internal hydraulic pressure increase, which demonstrates that existence of internal hydraulic pressure leads to the transformation from the quasi-brittle fracture to the brittle fracture of pre-flawed rock-like specimens in the triaxial compression tests.

The influence of flaw inclination angle on the mechanical and deformation behaviors of pre-flawed rock-like specimens under the fixed confining pressure of 8.0 MPa and internal hydraulic pressure of 2.0 MPa is investigated using four different types of rock-like

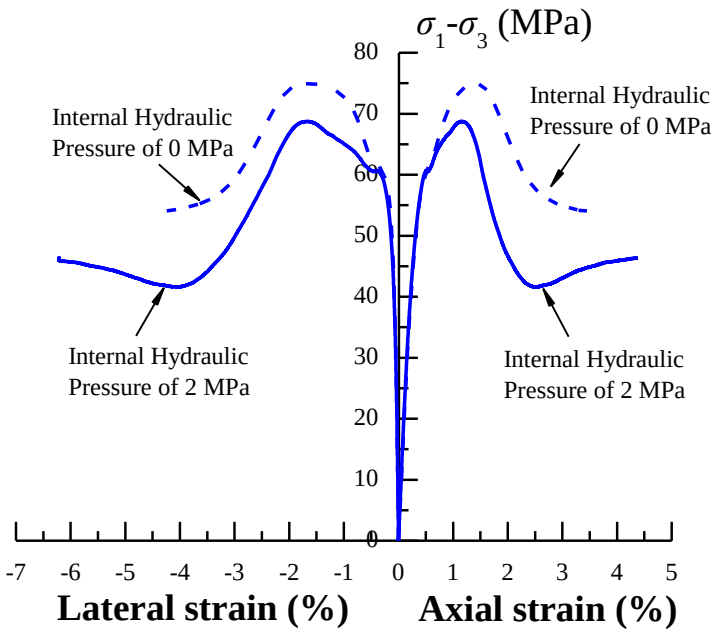

Fig. 4 Deviatoric stress–axial strain curves of the pre-flawed rock-like specimens in the conventional triaxial compression with confining pressures of 8.0 MPa

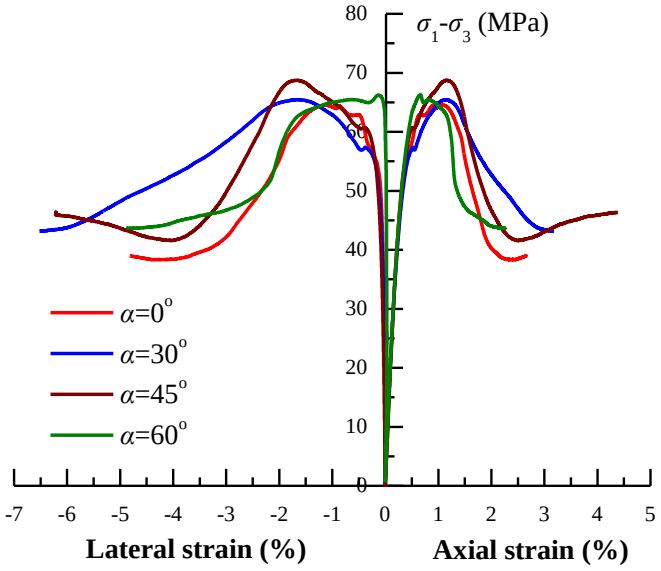

Fig. 5 Deviatoric stress–axial strain curves of the pre-flawed rock-like specimens subjected to both mechanical loads and internal hydraulic pressures ($\sigma_2 = \sigma_3 = 8$ MPa and $P_w = 2$ MPa)

cylindrical specimens containing a single pre-existing flaw with different inclination angles. The flaw inclination angles in four different types of pre-flawed rock-like specimen are 0°, 30°, 45° to 60°. The deviatoric stress–axial strain curves of the above four types of pre-flawed rock-like specimens with various inclination angle are plotted in Fig. 5. When the flaw inclination angle changes from 0° to 60°, the triaxial compressive strength first increases and then decreases, as shown in Fig. 5. When the flaw inclination angle is equal to 45°, it can be found from the triaxial compressive strength reaches the maximum. Similarly, the peak axial strain and peak lateral strain also first increase and then decreases, when the flaw inclination angle changes from 0° to 60°, as show in Fig. 5. For the post-peak deformation, when the flaw inclination angle changes from 0o to 30°, it can be observed from Fig. 5 that the degree of strain softening increases. While, when the flaw inclination angle changes from 30° to 60°, the degree of strain softening decreases, as shown in Fig. 5. These phenomena indicate that the brittle failure occurs in the pre-flawed rock-like specimen with large flaw inclination angle, and quasi-brittle failure happens in the pre-flawed rock-like

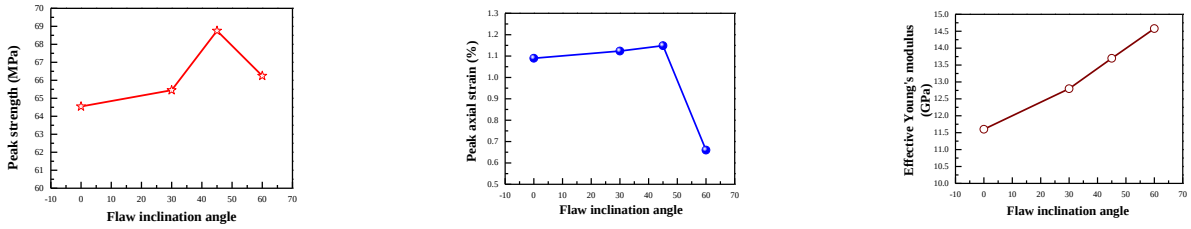

(a) Peak strength (b) Peak axial strain (c) Effective Young's modulus

Fig. 6. Influence of flaw inclination angle on the strength and deformability in pre-flawed rock-like materials under the coupled hydro-mechanical loading conditions

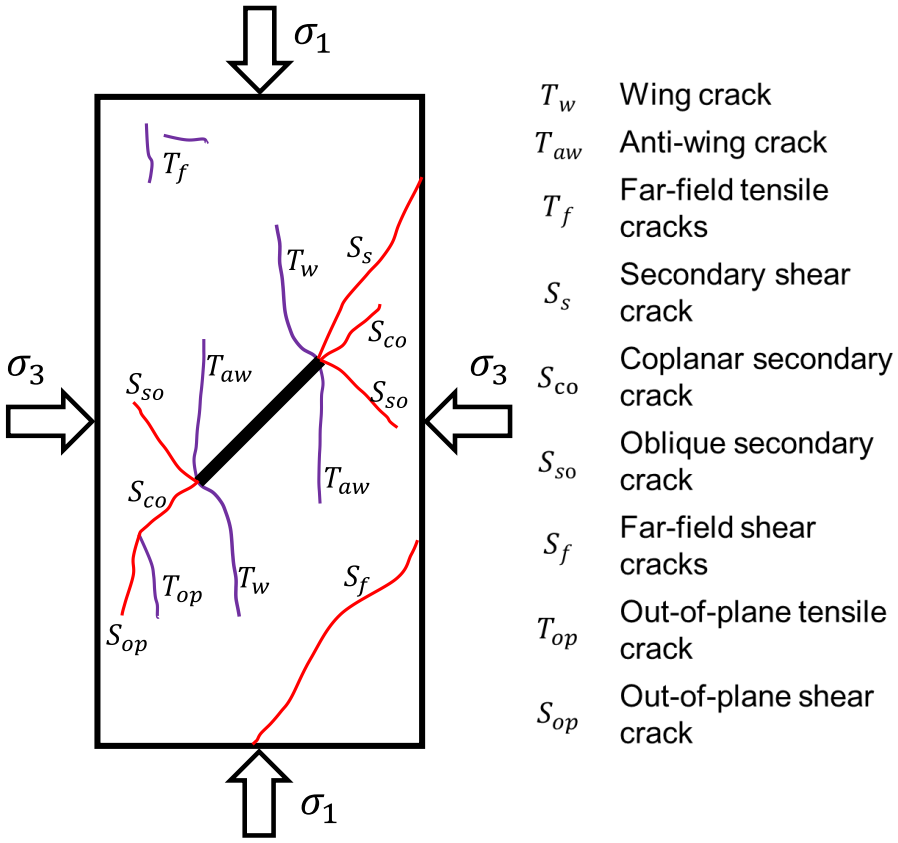

Fig. 7 A sketch of initiated crack types of fine-grained concretes specimens containing a single fissure under conventional triaxial compression modified by the reference (Yang and Huang 2017)

specimen with small flaw inclination angle under the fixed hydro-mechanical loading conditions.

The influences of flaw inclination angle on the peak strength, peak axial strain and the effective Young's modulus in the pre-flawed rock-like cylinder specimens under the coupled hydro-mechanical loading conditions are plotted in Fig. 6(a)-Fig. 6(c), respectively. As shown in Fig. 6(a), the peak strength of pre-flawed rock-like cylindrical specimen gradually increases as the inclination angle of the single pre-existing flaw increases from 0° to 45°. It can be also observed from Fig. 6(a) that when the flaw inclination angle increases from 45° to 60°, the peak strength of pre-flawed rock-like cylindrical specimens in the conventional triaxial compression decreases. With increasing flaw inclination angle from 0° to 45°, the peak axial strain slightly increases, as show in Fig. 6(b). It can also be observed from Fig. 6(b) that the peak axial strain sharply decreases as the flaw inclination angle varies from 45° to 60°. Furthermore, the effective Young's modulus of pre-flawed rock-like cylindrical specimens subjected to both mechanical loads and internal hydraulic pressures gradually increases with increasing the flaw inclination angle α, as shown in Fig. 6(c).

3.2 Fracture characteristics

To investigate the surface rock fracture characteristics and the ultimate failure modes in rock-like materials under the coupled hydro-mechanical loading conditions, nine different crack types are identified based on their geometries, and crack initiation and propagation mechanism based on the references (Wong and Einstein 2009; Yang and Huang 2017; Wang *et al.* 2017; Yang 2018), as shown in Fig. 7. It can be observed from Fig. 5 that there exist four

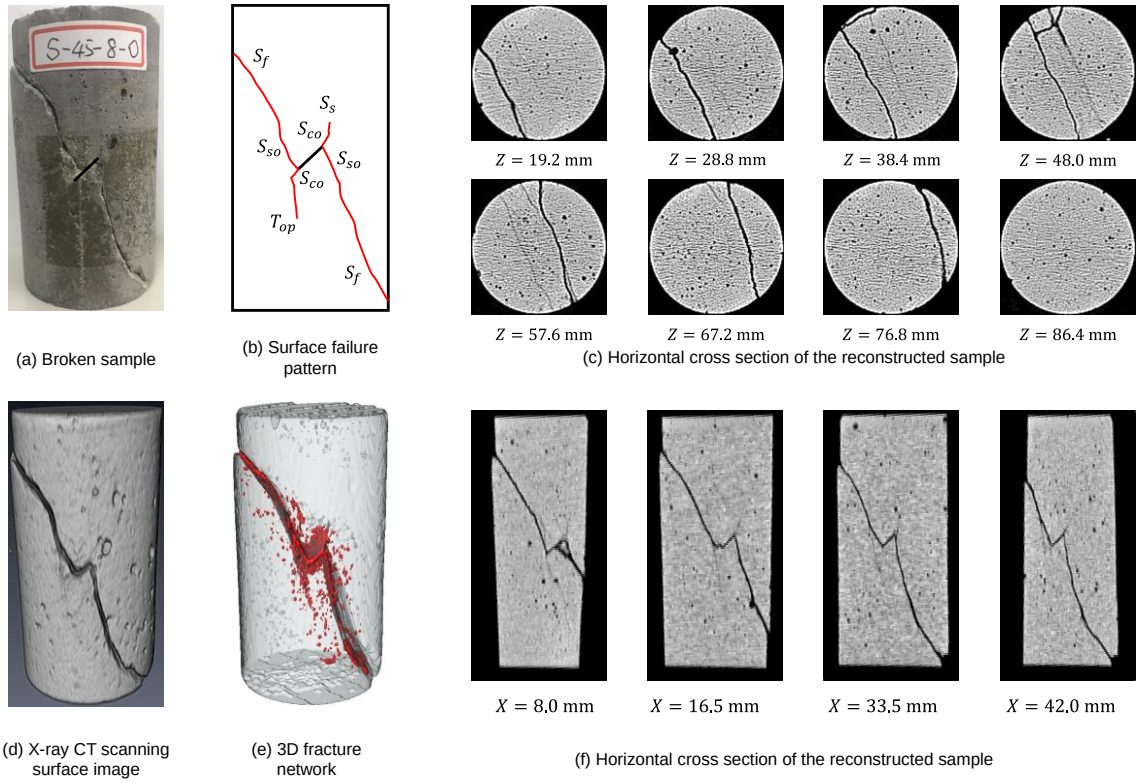

(a) Broken sample

(b) Surface failure pattern

(c) Horizontal cross section of the reconstructed sample

(d) X-ray CT scanning surface image

(e) 3D fracture network

(f) Horizontal cross section of the reconstructed sample

Fig. 8 Ultimate fracture patterns of pre-flawed rock-like specimen with flaw inclination angle of 45o under only mechanical loading obtained from X-ray computed tomography combined with 3-D reconstruction.

tensile types of cracks, i.e., wing crack (T_w), anti-wing crack (T_{aw}), far-field tensile crack (T_f) and out-of-plane tensile crack (T_{op}), and there are five shear types of cracks, including secondary crack (S_s), coplanar secondary crack (S_{co}), oblique secondary crack (S_{so}) far-field shear crack (S_f) and out-of-plane shear crack (S_{op}). The characteristics of different crack types can be found in the previous studies (Wong and Chau 1998; Wong and Einstein 2009; Yang *et al.* 2016; Yang 2018; Zhou *et al.* 2019; Wang *et al.*2019).

Based on the aforementioned nine different crack types, the ultimate surface failure modes of pre-flawed rock-like specimens containing a single pre-existing flaw with different inclination angle under the coupled hydro-mechanical loading conditions can be analyzed. Furthermore, in the present study, the failed rock-like specimens are carried out by the X-ray computed tomography (CT) scanning technique. For every broken rock-like specimen after the coupled hydro-mechanical loading conditions, the two-dimensional (2-D) slice images can be obtained by the X-ray CT scanning system. The consecutive 2-D images representing the linear distribution of X-ray attenuation can be reconstructed using Fourier

transformation of the projection data to show the 3-D image surfaces and 3-D fracture surfaces using the commercial software Avizo.

The ultimate failure modes of the above five types of failed rock-like specimens containing (see Table 2) under the coupled hydro-mechanical loading conditions are performed in Figs. 8-12. Every figure of Figs. 8-12 is composed of six different subfigures, including (a) really broken sample, (b) surface failure pattern, (c) the representative horizontal cross section X-ray CT scanning images (d) X-ray CT scanning surface image, (e) 3-D reconstructed fracture network and (f) the representative vertical cross section X-ray CT scanning images.

In Figs. 8-12, the comparisons of the X-ray CT scanning surface images and the actual surface crack photographs of pre-flawed rock-like cylindrical specimens after the coupled hydro-mechanical loading conditions are presented. The black regions in the X-ray CT scanning surface images represent cracks or surface spalling and other regions indicate no surface failure. It can be found from Figs. 8-12 that the X-ray CT scanning surface images are in agreement with the actual surface crack photographs, which illustrates that X-ray CT scanning system can be used to explore the extent of internal damage in rock-like specimens after the coupled hydro-mechanical loading. In Figs. 8-12, the horizontal cross-sections with different heights and vertical cross-sections with various depths of failed specimens after the coupled hydro-mechanical loading conditions are shown to illustrate the internal damage characteristics. Futhermore, the 3-D fracture networks of the failed specimens obtained by the X-ray CT scanning images combined with 3-D reconstruction technique are also performed in Figs. 8-12. The 3-D reconstructioned fracture networks provide the fracture surfaces in the 3-D spatial distributions of the broken samples after the coupled hydro-mechanical loading.

3.3 Internal hydraulic pressure effect

To illustrate the internal hydraulic pressure effect on the

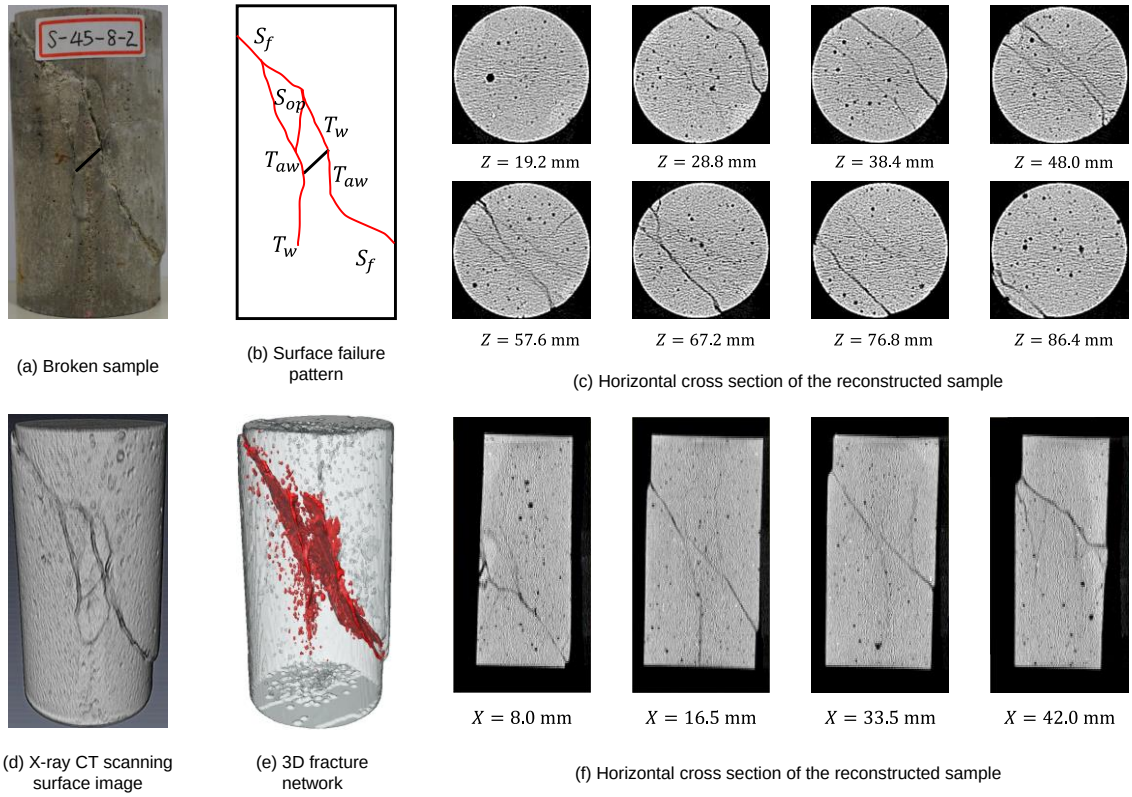

(a) Broken sample

(b) Surface failure pattern

(c) Horizontal cross section of the reconstructed sample

(d) X-ray CT scanning surface image

(e) 3D fracture network

(f) Horizontal cross section of the reconstructed sample

Fig. 9 Ultimate fracture patterns of pre-flawed rock-like specimen with flaw inclination angle of 45° under the coupled hydro-mechanical loading conditions obtained from X-ray computed tomography combined with 3-D reconstruction.

failure characteristics of rock-like materials, the failure patterns in Type-I pre-flawed rock-like specimen and Type-II pre-flawed rock-like specimens in Table 2 are firstly compared. For Type-I and Type-II pre-flawed rock-like specimens, the flaw inclination angle and confining pressure are fixed as 45° and 8.0 MPa, respectively. The ultimate failure mode of pre-flawed rock-like specimen containing a single flaw with inclination angle of 45° subjected to only mechanical loads, i.e., Type-I specimen, are plotted in Fig. 8. It can be found from Fig. 8 that the coplanar secondary cracks are initiated from the flaw tips and propagate along the direction of the initial flaw. Meanwhile, the oblique secondary cracks are also initiated from the flaw tips and grow along the direction perpendicular to the original flaw, as shown in Fig. 8. The far field shear cracks coalesce with the oblique secondary cracks, which results in the ultimate shear failure mode of the pre-flawed rock-like specimen with $\alpha = 45°$, as shown in Fig. 8.

For the pre-flawed rock-like specimen containing a single flaw with inclination angle of 45° subjected to both mechanical loads and the internal hydraulic pressure, i.e., Type-II specimen, the associated ultimate failure modes are plotted in Fig. 9. It can be observed from Fig. 9 that the wing cracks and anti-wing cracks are initiated from flaw tips. The coalescences of wing cracks, anti-wing cracks and far field shear cracks lead to the mixed tensile-shear failure mode in pre-flawed rock-like specimens under the hydro-mechanical loading conditions. From the 3-D reconstructed fracture networks of two different types of broken specimens, it can be found from Fig. 8 and Fig. 9 that the internal hydraulic pressure leads to the complicated fracture surfaces in the spatial distributions, and the internal hydraulic pressure contributes to the complicated failure modes.

3.4 Flaw inclination angle effect

To investigate the flaw inclination angle effect on the fracture characteristics of pre-flawed rock-like specimens under the coupled hydro-mechanical loading conditions, the ultimate fracture modes of four different types of broken rock-like specimens, i.e., Type-II, Type-III, Type-IV and Type-V in Table 2, are performed.

For the pre-flawed rock-like specimen with $\alpha = 0°$, i.e., Type-III specimen, the corresponding failure mode of broken rock-like specimen are shown in Fig. 10. The wing cracks and anti-wing cracks are initiated from the flaw tips and propagate along the major principle direction. It can be found from Fig. 10 that the wing cracks coalesce with the far field shear cracks, and the anti-wing cracks link with the out-of-plane shear crack and the far field shear crack. The coalescence of cracks in the pre-flawed rock-like specimen with $\alpha = 0°$ results in the mixed tensile-shear failure modes.

For the pre-flawed rock-like specimen with $\alpha = 30°$, i.e., Type-III specimen, the associated failure mode of broken rock-like specimen are shown in Fig. 11. Wing cracks and anti-wing cracks are initiated from the flaw tips.

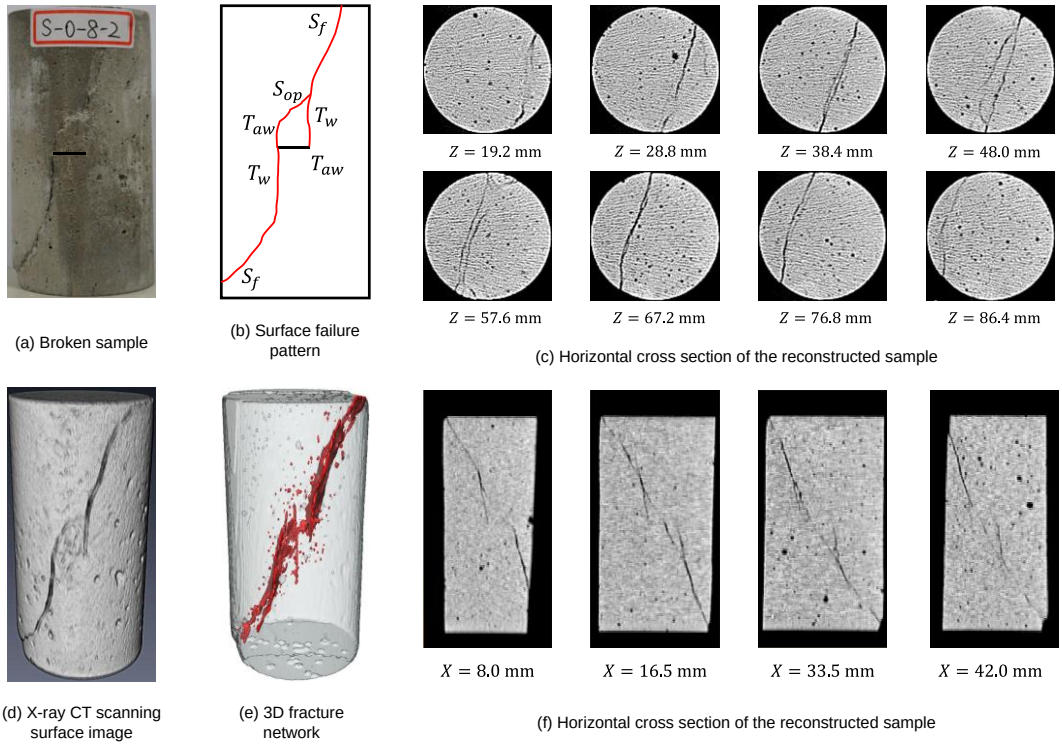

(a) Broken sample (b) Surface failure pattern (c) Horizontal cross section of the reconstructed sample

(d) X-ray CT scanning surface image (e) 3D fracture network (f) Horizontal cross section of the reconstructed sample

Fig. 10 Ultimate fracture patterns of pre-flawed rock-like specimen with flaw inclination angle of 0° obtained from X-ray computed tomography combined with 3-D reconstruction

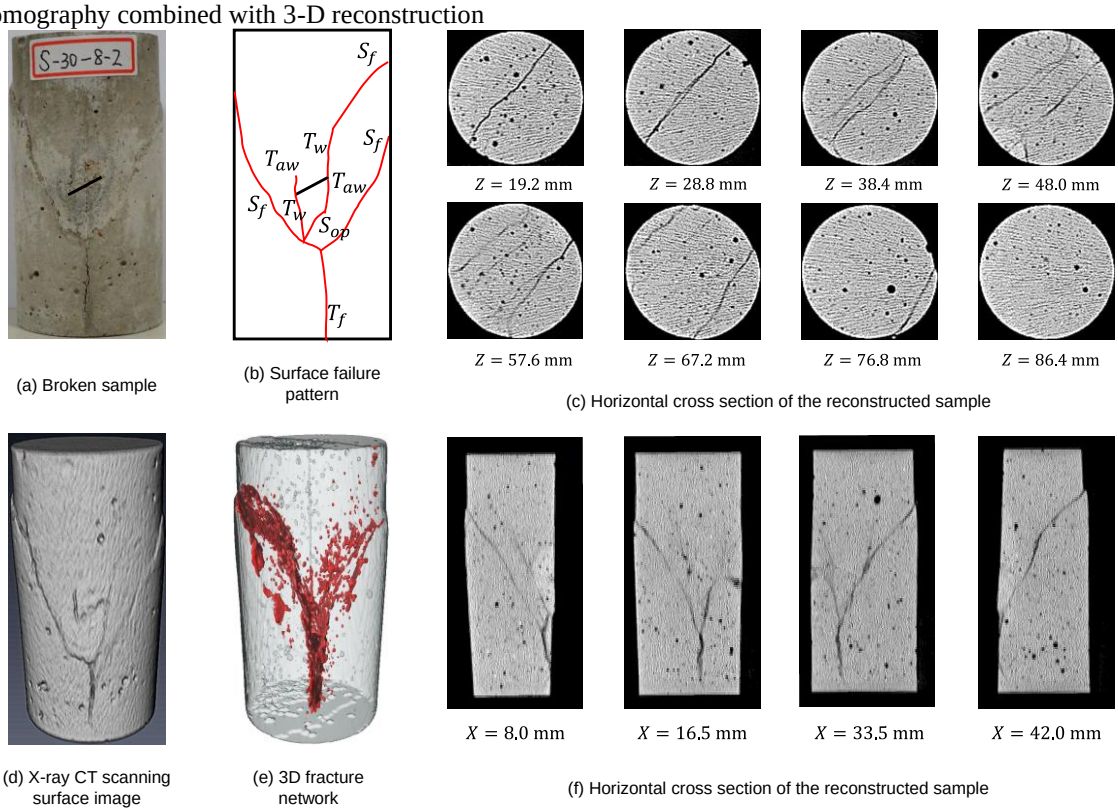

(a) Broken sample (b) Surface failure pattern (c) Horizontal cross section of the reconstructed sample

(d) X-ray CT scanning surface image (e) 3D fracture network (f) Horizontal cross section of the reconstructed sample

Fig. 11 Ultimate fracture patterns of pre-flawed rock-like specimen with flaw inclination angle of 30° obtained from X-ray computed tomography combined with 3-D reconstruction.

The anti-wing crack and wing crack are coalesced with each other by the out-of-plane shear cracks. The far field shear cracks link with the far field tensile crack, which results in the mixed tensile-shear failure mode, as shown in Fig. 11.

For the pre-flawed rock-like specimen with $\alpha = 60°$, i.e., Type-III specimen, the corresponding failure mode of broken rock-like specimen are shown in Fig. 12. It can be found from Fig. 12 that wing cracks initiated from the flaw tip are linked with the oblique secondary cracks by the out-

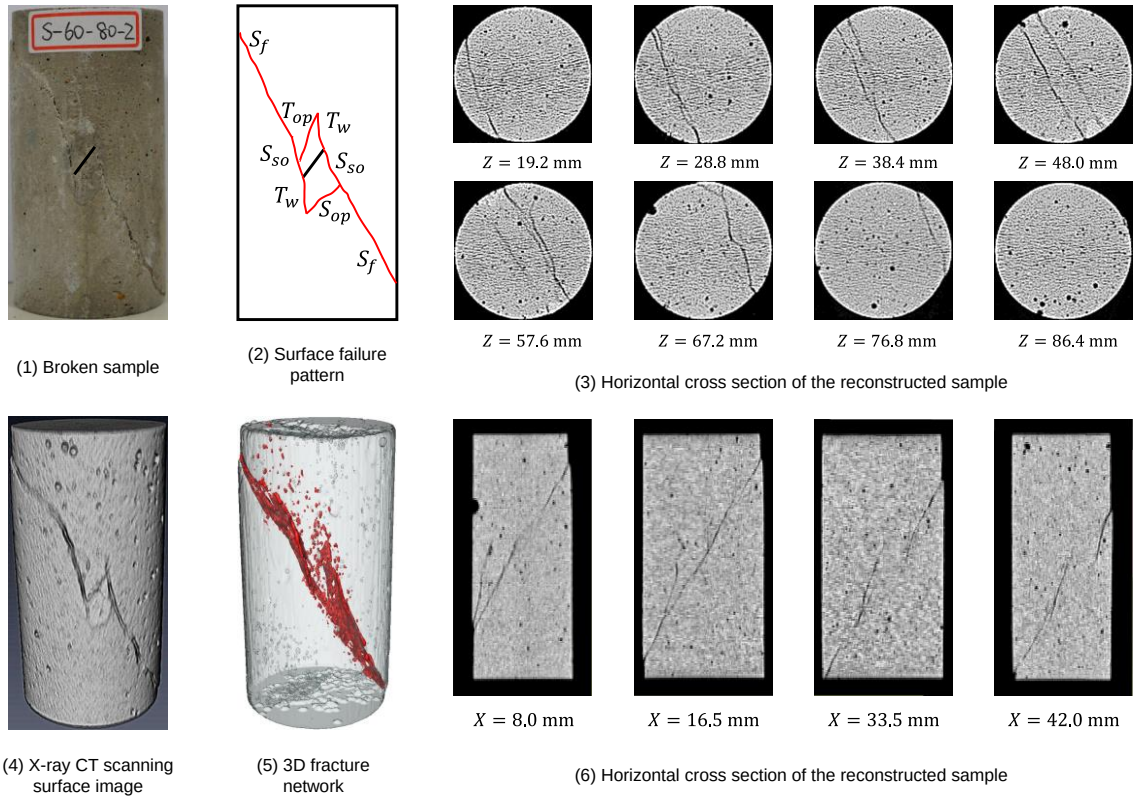

Fig. 12 Ultimate fracture patterns of pre-flawed rock-like specimen with flaw inclination angle of 60° obtained from X-ray computed tomography combined with 3-D reconstruction.

of-plane tensile cracks at the region around the pre-existing flaw in the pre-flawed rock-like cylindrical specimen subjected to both mechanical loads and the internal hydraulic pressure. The coalescence of the oblique secondary cracks and far field shear cracks leads to the ultimate failure patterns of pre-flawed rock-like specimen with $\alpha = 60°$, which results in the pure shear failure mode, as shown in Fig. 12.

From the aforementioned analysis, when the flaw inclination angle varies from 0° to 60° in the pre-flawed rock-like specimens under the fixed confining pressures and internal hydraulic pressures, the ultimate failure mode transform from the mixed tensile-shear failure mode to the pure shear failure mode, as shown in Figs. 9-12. The 3-D reconstructed fracture surfaces demonstrate the internal failure characteristics of the mixed tensile-shear failure modes are much more complicated than those of the pure shear failure modes, as shown in Figs. 9-12.

4. Conclusions

In the present research, the influence of flaw inclination angle on fracture behaviors in pre-flawed rock-like materials subjected to both mechanical loads and the internal hydraulic pressures are experimentally carried out using the X-ray computed tomography combined with 3-D reconstruction technique. The current experimental results not only illustrate the mechanical and deformation behaviors, but also reveal the internal fracture characteristics of rock-like materials under the coupled hydro-mechanical loading conditions. Based on the experimental results, the following conclusions can be obtain

- The X-ray computed tomography technique combined with 3-D reconstruction successfully provides the internal fracture characteristics in pre-fissured rock-like specimens under the coupled hydro-mechanical loading. The ultimate fracture surfaces in spatial distributions can be revealed as curve surfaces by this technique.
- The internal hydraulic pressure contributes to the initiation and propagation of tensile cracks, such as wing cracks and anti-wing cracks, in rock-like materials. It can be found from experimental results that the inclined angles of 3-D fracture surfaces in rock-like materials under the only mechanical loading with respect to the axial direction are larger than those in rock-like materials under the coupled hydro-mechanical loading. Furthermore, internal hydraulic pressures also contribute to the mixed tensile-shear crack coalescence around the pre-existing flaw tips in the internal rock-like specimens.
- For the fixed confining pressures and internal hydraulic pressures, the experimental results demonstrate that the peak strength of pre-flawed rock-like specimens first increases and then decreases as the flaw inclination angle in rock-like specimens subjected to both the mechanical and internal hydraulic loads increases from 0° to 60°. Moreover, the peak axial strain in the pre-flawed rock-like specimens under the coupled hydro-mechanical loading first gradually increases as the flaw inclination angle

increases from 0º to 45º. When the flaw inclination angle increases from 45º to 60º, the peak axial strain sharply decreases in the pre-flawed rock-like specimens subjected to both the mechanical loads and internal hydraulic pressures. Furthermore, when the flaw inclination angle increases from 0º to 60º, the effective Young's modulus gradually increases in the pre-flawed rock-like specimens under the coupled hydro-mechanical loading conditions.

- When the confining pressures and internal hydraulic pressures are fixed, the X-ray computed tomography images and the reconstructed 3-D fracture surfaces indicate the ultimate failure mode of pre-flawed rock-like specimens transforms from the mixed tensile-shear failure mode to the pure shear failure modes as the inclination angle of pre-existing flaw increases. In addition, with increasing the flaw inclination in rock-like specimens subjected to both the mechanical loads and internal hydraulic pressures, the crack coalescence around the pre-existing flaw tips are mainly belong to the mixed tensile-shear type.

Acknowledgments

This work is supported by National Natural Science Foundation of China (Grant Nos. 41972266; 41772319; 51674151), National Key Research and Development Program of China (Grant No. 2018YFC1504802), and Fundamental Research Funds for the Central Universities of China (Grant No. 2019CDCG0013) which are gratefully acknowledged.

References

Bobet, A. and Einstein, H.H. (1998), "Fracture coalescence in rock-type material under uniaxial and biaxial compression", *Int. J. Rock Mech. Min. Sci.,* **35**(7), 863-888. https://doi.org/10.1016/S0148-9062(98)00005-9.

Christe, P., Turberg, P., Labious, V., Meuli, R. and Parriaux, A. (2011), "An X-ray computed tomography-based index to characterize the quality of cataclastic carbonate rock samples", *Eng. Geol.,* **117,** 180-188. https://doi.org/10.1016/j.enggeo.2010.10.016.

Cai, X., Zhou, Z., Liu, K., Du, X. and Zhang, H. (2019), "Water-Weakening Effects on the Mechanical Behavior of Different Rock Types: Phenomena and Mechanisms", *Appl. Sci.,* **9**(20), 4450. https://doi.org/10.3390/app9204450.

Cao, R. H., Cao, P., Lin, H., Ma, G.W., X., Fan and Xiong, X.G. (2018), "Mechanical behavior of an opening in a jointed rock-like specimen under uniaxial loading: Experimental studies and particle mechanics approach", *Arch. Civ. Mech. Eng.,* **18**(1), 198-214. https://doi.org/10.1016/j.acme.2017.06.010.

Cała, M., Cyran, K., Stopkowicz, A., Kolano, M. and Szczygielski, M. (2016), "Preliminary Application of X-ray Computed Tomograph on Characterisation of Polish Gas Shale Mechanical Properties", *Rock Mech. Rock Eng.,* **49**(12), 4935-4943. https://doi.org/10.1007/s00603-016-1045-6.

Diaz, M., Kim, K.Y., Yeom, S., Zhuang, L., Park, S. and Min, K.B. (2017), "Surface roughness characterization of open and closed rock joints in deep cores using X-ray computed tomography", *Int. J. Rock Mech. Min. Sci.,* **98,** 10-19. https://doi.org/10.1016/j.ijrmms.2017.07.001.

Einstein, H.H. and Hirschfeld, R.C. (1973), "Model studies on mechanics of jointed rock", *J. Soil Mech. Found. Div. ASCE,* **99,** 229-248.

Feng, X.T., Chen, S.L. and Zhou H. (2004), "Real-time computerized tomography (CT) experiments on sandstone damage evolution during triaxial compression with chemical corrosion", *Int. J. Rock Mech. Min. Sci.,* **41**(2), 181-192. https://doi.org/10.1016/S1365-1609(03)00059-5.

Ge, X.R., Ren, J.X., Pu, Y.B., Ma, G.W. and Zhu, Y.L. (2001), "Real-in time CT test of the rock meso-damage propagation law", *Sci. China (Ser. E),* **44**(3), 328-336. https://doi.org/10.1007/BF02916710.

Haeri, H., Sarfarazi, V. and Zhu, Z. (2018), "Numerical simulation of the effect of bedding layer geometrical properties on the punch shear test using PFC3D", *Struct. Eng. Mech.,* **68**(4), 507-517. https://doi.org/10.12989/sem.2018.68.4.507.

Haeri, H., Sarfarazi, V., Zhu, Z. and Moosavi, E. (2019a), "Effect of transversely bedding layer on the biaxial failure mechanism of brittle materials", *Struct. Eng. Mech.,* **69**(1), 11-20. https://doi.org/10.12989/sem.2019.69.1.011.

Haeri, H., Sarfarazi, V., Zhu, Z. and Marji, MF. (2019b), "Experimental and numerical studies of the pre-existing cracks and pores interaction in concrete specimens under compression", *Smart Struct. Syst.,* **23**(5), 479-493. https://doi.org/10.12989/sss.2019.23.5.479.

Hirono, T., Takahashi, M. and Nakashima, S. (2003), "In situ visualization of fluid flow image within deformed rock by X-ray CT", *Eng. Geol.,* **70,** 37-46. https://doi.org/10.1016/S0013-7952(03)00074-7.

Huang, Y.H., Yang, S.Q., Tian, W.L., Zhao, J., Ma, D. and Zhang, C.S. (2017a), "Physical and mechanical behavior of granite containing pre-existing holes after high temperature treatment", *Arch. Civ. Mech. Eng.,* **17**(4), 912-925. https://doi.org/10.1016/j.acme.2017.03.007.

Huang, S., Liu, D., Yao, Y., Gan, Q., Cai, Y. and Xu, L.(2017b), "Natural fractures initiation and fracture type prediction in coal reservoir under different in-situ stresses during hydraulic fracturing", *J. Nat. Gas. Sci. Eng.,* **43,** 69-80. https://doi.org/10.1016/j.jngse.2017.03.022.

Huang, Y.H. and Yang, S.Q. (2018a), "Mechanical and cracking behavior of granite containing two coplanar flaws under conventional triaxial compression", *Int. J. Damage Mech.,* **28**(4), 590-610. https://doi.org/10.1177/1056789518780214.

Huang, Y.H., Yang, S.Q., Hall, M.R., Tian, W.L. and Yin, P.F. (2018b), "Experimental study on uniaxial mechanical properties and crack propagation in sandstone containing a single oval cavity", *Arch. Civ. Mech. Eng.,* **18**(4), 1359-1373. https://doi.org/10.1016/j.acme.2018.04.005.

Kawakata, H., Cho, A., Kiyama, T., T. Yanagidani, K. Kusunose, M. Shimada(1999), "Three-dimensional observations of faulting process in Westerly granite under uniaxial and triaxial conditions by X-ray CT scan", *Tectonophysics,* **313**(3), 293-305. https://doi.org/10.1016/S0040-1951(99)00205-X.

Kou, M.M., Liu, X.R., Tang, S.D. and Wang, Y. (2019a), "3-D X-ray Computed Tomography on Failure Characteristics of Rock-like Materials under Coupled Hydro-Mechanical Loading", *Theor. Appl. Fract. Mech.,* **104**, 102396. https://doi.org/10.1016/j.tafmec.2019.102396.

Kou, M., Han, D., Xiao, C. and Wang, Y. (2019b), "Dynamic fracture instability in brittle materials: Insights from DEM simulations", *Struct. Eng. Mech.,* **71**(1), 65-75. https://doi.org/10.12989/sem.2019.71.1.065.

Kou, M., Lian, Y.J. and Wang, Y.T. (2019c), "Numerical investigations on crack propagation and crack branching in brittle solids under dynamic loading using bond-particle model", Eng. Fract. Mech., 212, 41-56.

Li, X. and Chen, J. (2016), "An extended cohesive damage model for simulating multicrack propagation in fibre composites",

Compos. Struct., **143**, 1-8. https://doi.org/10.1016/j.compstruct.2016.02.026.

Li, X. and Chen, J. (2017a), "An extended cohesive damage model for simulating arbitrary damage propagation in engineering materials", *Comput. Methods Appl. Mech. Engrg.,* **315,** 744-759. https://doi.org/10.1016/j.cma.2016.11.029.

Li, X., and Chen, J. (2017b), "A highly efficient prediction of delamination migration in laminated composites using the extended cohesive damage model", *Compos. Struct.*, **160**, 712-721. https://doi.org/10.1016/j.compstruct.2016.10.098.

Liu, Y., Dai, F., Dong, L., Xu, N. and Feng, P. (2018), "Experimental investigation on the fatigue mechanical properties of intermittently jointed rock models under cyclic uniaxial compression with different loading parameters", *Rock Mech. Rock Eng.,* **51**(1), 47-68. https://doi.org/10.1007/s00603-017-1327-7.

Meier, T., Rybacki, E., Backers, T. and Dresen, G. (2015), "Influence of bedding angle on borehole stability: a laboratory investigation of transverse isotropic oil shale", *Rock Mech. Rock Eng.,* **48**(4), 1535-1546. https://doi.org/10.1007/s00603-014-0654-1.

Sarfarazi, V. and Haeri, H. (2018), "Three-dimensional numerical modeling of effect of bedding layer on the tensile failure behavior in hollow disc models using Particle Flow Code (PFC3D)", *Struct. Eng. Mech.,* **68**(5), 537-547. https://doi.org/10.12989/sem.2018.68.5.537.

Song, Z., Konietzky, H. and Frühwirt, T. (2018), "Hysteresis energy-based failure indicators for concrete and brittle rocks under the condition of fatigue loading", *Int J Fatigue,* **114,** 298-310. https://doi.org/10.1016/j.ijfatigue.2018.06.001.

Song, Z., Konietzky, H. and Herbst, M. (2019a), "Bonded-particle model-based simulation of artificial rock subjected to cyclic loading", *Acta Geotech.,* **14,** 955-971. https://doi.org/10.1007/s11440-018-0723-9.

Song, Z., Frühwirt, T. and Konietzky, H. (2019b), "Inhomogeneous mechanical behaviour of concrete subjected to monotonic and cyclic loading", *Int J Fatigue,* 105383. https://doi.org/10.1016/j.ijfatigue.2019.105383.

Silva, B.G.D. and Einstein, H.H. (2014), "Finite element study of fracture initiation in flaws subject to internal fluid pressure and vertical stress". *Int. J. Solids Struct.,* **51**(23-24), 4122-4136. https://doi.org/10.1016/j.ijsolstr.2014.08.006.

Sufian, A., Russell, A.R. (2013), "Microstructural pore changes and energy dissipation in Gosford sandstone during pre-failure loading using X-ray CT", *Int. J. Rock Mech. Min. Sci.,* **57,** 119-131. https://doi.org/10.1016/j.ijrmms.2012.07.021.

Wang, Y., Zhou, X. and Xu, X. (2016), "Numerical simulation of propagation and coalescence of flaws in rock materials under compressive loads", *Eng. Fract. Mech.,* **163**, 248-273. https://doi.org/10.1016/j.engfracmech.2016.06.013.

Wang, L., Xu, J. and Wang, J. (2017a), "Static and dynamic Green's functions in peridynamics", J. Elast., **126,** 95-125. https://doi.org/10.1007/s10659-016-9583-4.

Wang, Y., Zhou, X., Shou, Y. (2017b), "The modeling of crack propagation and coalescence in rocks under uniaxial compression using the novel conjugated bond-based peridynamics", *Int. J. Mech. Sci.,* **128**, 614-643. https://doi.org/10.1016/j.ijmecsci.2017.05.019.

Wang, Y., Li, C.H., Hao, J. and Zhou, R.Q. (2018a), "X-ray micro-tomography for investigation of meso-structural changes and crack evolution in Longmaxi formation shale during compressive deformation", *J. Petrol. Sci. Eng,* **164**, 278-288. https://doi.org/10.1016/j.petrol.2018.01.079.

Wang, Y., Zhou, X., Wang, Y. and Shou, Y. (2018b), "A 3D conjugated bond-pair-based peridynamic formulation for initiation and propagation of cracks in brittle solids", *Int. J. Solids Struct.,* **134,** 89-115. https://doi.org/10.1016/j.ijsolstr.2017.10.022.

Wang, L. and Abeyaratne, R. (2018c), "A one-dimensional peridynamic model of defect propagation and its relation to certain other continuum models", *J. Mech. Phys. Solids,* **116,** 334-349. https://doi.org/10.1016/j.jmps.2018.03.028.

Wang, Y., Liu, B. and Qi, Y. (2018), "A Risk Evaluation Method with an Improved Scale for Tunnel Engineering", *Abab. J. Sci. Eng.,* **43,** 2053-2067. https://doi.org/10.1007/s13369-017-2974-4.

Wang, Y., Li, C.H. and Hu, Y.Z. (2019a), "3D image visualization of meso-structural changes in a bimsoil under uniaxial compression using X-ray computed tomography (CT)", *Eng. Geol.,* **248**, 61–69. https://doi.org/10.1016/j.enggeo.2018.11.004.

Wang, Y., Zhou, X. and Kou, M. (2019b), "An improved coupled thermo-mechanic bond-based peridynamic model for cracking behaviors in brittle solids subjected to thermal shocks", *Eur. J. Mech. A-Solid,* **73**, 282-305. https://doi.org/10.1016/j.euromechsol.2018.09.007.

Wang, Y.T., Zhou, X.P. and Kou, M.M. (2019c), "Three-dimensional numerical study on the failure characteristics of intermittent fissures under compressive-shear loads", *Acta Geotech.,* **14**(4), 1161-1193. https://doi.org/10.1007/s11440-018-0709-7.

Wang, L., Xu, J., Wang, J. and Karihaloo, B.L. (2019d), "A mechanism-based spatiotemporal non-local constitutive formulation for elastodynamics of composites", *Mech. Mater.,* **128,** 105-116. https://doi.org/10.1016/j.mechmat.2018.07.013.

Wang, S., Li, X., Yao, J., Gong, F., Li, X., Du, K., Tao, M., Huang, L. and Du, S. (2019e), "Experimental investigation of rock breakage by a conical pick and its application to non-explosive mechanized mining in deep hard rock", *Int. J. Rock Mech. Min. Sci.,* **122,** 104063. https://doi.org/10.1016/j.ijrmms.2019.104063.

Wang, L. and Wang, J. (2019f), "On the Invariance of Governing Equations of Current Nonlocal Theories of Elasticity Under Coordinate Transformation and Displacement Gauge Change", *J. Elast.,* **137,** 237-246. https://doi.org/10.1007/s10659-018-09715-7.

Wang, S., Huang, L. and Li, X. (2020), "Analysis of rockburst triggered by hard rock fragmentation using a conical pick under high uniaxial stress", *Tunnel. Undergr. Sp. Tech.,* **96,** 103195. https://doi.org/10.1016/j.tust.2019.103195.

Wong, R.H.C. and Chau, K.T. (1998), "Crack coalescence in a rock-like material containing two cracks", *Int. J. Rock Mech. Min. Sci.,* **35**(2), 147-164. https://doi.org/10.1016/S0148-9062(97)00303-3.

Wong, L.N.Y. and Einstein, H.H. (2009), "Crack coalescence in molded gypsum and Carrara marble: part I. Macroscopic observations and interpretation", *Rock Mech. Rock Eng.,* **42**(3), 475-511. https://doi.org/10.1007/s00603-008-0002-4.

Yang, S.Q., Ju, Y., Gao, F. and Gui, Y.L. (2016), "Strength, deformability and X-ray micro-CT observations of deeply buried marble under different confining pressures", *Rock Mech. Rock Eng.,* **49**(11), 4227-4244. https://doi.org/10.1007/s00603-016-1040-y.

Yang, S.Q. and Huang, Y.H. (2017), "An experimental study on deformation and failure mechanical behavior of granite containing a single fissure under different confining pressures", *Environ. Earth Sci.,* **76**(10), 364. https://doi.org/10.1007/s12665-017-6696-4.

Yang, S.Q. (2018), "Fracturing mechanism of compressed hollow‐cylinder sandstone evaluated by X-ray micro-CT scanning", *Rock Mech. Rock Eng.,* **51**(7), 2033-2053. https://doi.org/10.1007/s00603-018-1466-5.

Yu, L. and Pan, B. (2017), "Color stereo-digital image correlation method using a single 3CCD color camera", *Exp. Mech.,* **57**(4), 649-657. https://doi.org/10.1007/s11340-017-0253-7.

Yu, L., Tao, R. and Lubineau, G. (2019), "Accurate 3D shape,

displacement and deformation measurement using a smartphone", *Sensors*, **19**(3), 719. https://doi.org/10.3390/s19030719.

Yun, T.S., Jeong, Y.J., Kim, K.Y. and Min, K.B. (2013), "Evaluation of rock anisotropy using 3D X-ray computed tomography", *Eng. Geol.,* **163,** 11-19. https://doi.org/10.1016/j.enggeo.2013.05.017.

Zhao, G.F., Russell, A.R., Zhao, X. and Khalili, N. (2014), "Strain rate dependency of uniaxial tensile strength in Gosford sandstone by the Distinct Lattice Spring Model with X-ray micro CT", *Int. J. Solids Struct.,* **51,** 1587-1600. https://doi.org/10.1016/j.ijsolstr.2014.01.012.

Zhang, R., Ai, T., Ren, L. and Li, G. (2019), "Failure characterization of three typical coal-bearing formation rocks using acoustic emission monitoring and X-ray computed tomography techniques", *Rock Mech. Rock Eng.,* **52**(6), 1945-1958. https://doi.org/10.1007/s00603-018-1677-9.

Zhou, X.P., Zhang, Y.X. and Ha, Q.L. (2008), "Real-time computerized tomography (CT) experiments on limestone damage evolution during unloading", *Theor. Appl. Fract. Mech.,* **50(1),** 49-56. https://doi.org/10.1016/j.tafmec.2008.04.005.

Zhou, X.P., Cheng, H. and Feng, Y.F. (2014), "An Experimental Study of Crack Coalescence Behaviour in Rock-like Materials Containing Multiple Flaws Under Uniaxial Compression", *Rock Mech. Rock Eng.,* **47**(6), 1961-1986. https://doi.org/10.1007/s00603-013-0511-7.

Zhuang, X., Chun, J. and Zhu, H. (2014), "A comparative study on unfilled and filled crack propagation for rock-like brittle material", *Theor. Appl. Fract. Mech.,* **72,** 110-120. https://doi.org/10.1016/j.tafmec.2014.04.004.

Zhou, X.P., Wang, Y.T., Zhang, J.Z. and Liu, F.N. (2019), "Fracturing behavior study of three-flawed specimens by uniaxial compression and 3D digital image correlation: sensitivity to brittleness", *Rock Mech. Rock Eng.,* **52**(3), 691-718. https://doi.org/10.1007/s00603-018-1600-4.

Zhou, Z., Cai, X., Ma, D., Chen, L., Wang, S. and Tan L. (2018), "Dynamic tensile properties of sandstone subjected to wetting and drying cycles", *Constr. Build Mater.,* **182:** 215-232. https://doi.org/10.1016/j.conbuildmat.2018.06.056.

Zhou, Z., Cai, X., Li, X., Cao, W. and Du, X. (2019), "Dynamic Response and Energy Evolution of Sandstone Under Coupled Static–Dynamic Compression: Insights from Experimental Study into Deep Rock Engineering Applications", *Rock Mech. Rock Eng*., 1-27. https://doi.org/10.1007/s00603-019-01980-9.

CC